metals

MDPI

Article

Synthesis of Low-Crystalline MnO_2/MXene Composites for Capacitive Deionization with Efficient Desalination Capacity

Zhumei Sun [1], Jun Peng [2], Shu Yang [3], Riya Jin [1], Changcheng Liu [1] and Que Huang [1,*]

[1] School of Environmental and Safety Engineering, North University of China, Taiyuan 030051, China; sunzhumei41@163.com (Z.S.); jrya@nuc.edu.cn (R.J.); ccliu@nuc.edu.cn (C.L.)
[2] Changsha Research Institute of Mining and Metallurgy Co., Ltd., Changsha 410012, China; pengjgy@163.com
[3] College of Environment and Safety Engineering, Qingdao University of Science and Technology, Qingdao 266042, China; ys131350@163.com
* Correspondence: que.huang@nuc.edu.cn

Abstract: MXene has drawn widespread attention as a potential material for electrode use in capacitive deionization (CDI). However, the applications of MXene are limited by its property of low electrical capacity. Herein, a MnO_2/MXene composite was firstly evaluated in a capacitive deionization system, in which the MnO_2 acts as intercalation-type pseudocapacitive electrodes to enhance the electrical capacity, and MXene provides an electron conduction highway network that improves the charge transfer of the MnO_2. The result showed that the low-crystallinity MnO_2 with irregular particles was well-distributed on the surface of the MXene. The desalination capacity of 30.5 $mg \cdot g^{-1}$ is achieved at a voltage window of 1.2 V, which was higher than that of the reported pure MXene and MnO_2. The electrical double-layer (EDL) capacitive and the diffusion-controlled processes are the main charge storage mechanisms, and the EDL contribution provides 50.3% to the total capacitance. This result suggests a promising direction for further applying a MnO_2/MXene composite in CDI.

Keywords: capacitive deionization; MXene; MnO_2; desalination; low crystallinity

check for updates

Citation: Sun, Z.; Peng, J.; Yang, S.; Jin, R.; Liu, C.; Huang, Q. Synthesis of Low-Crystalline MnO_2/MXene Composites for Capacitive Deionization with Efficient Desalination Capacity. *Metals* **2023**, *13*, 1047. https://doi.org/10.3390/met13061047

Academic Editor: Jean-Louis Bobet

Received: 31 March 2023
Revised: 12 May 2023
Accepted: 13 May 2023
Published: 30 May 2023

Copyright: © 2023 by the authors. Licensee MDPI, Basel, Switzerland. This article is an open access article distributed under the terms and conditions of the Creative Commons Attribution (CC BY) license (https://creativecommons.org/licenses/by/4.0/).

1. Introduction

Freshwater scarcity brought on by population growth and economic needs has grown into a serious problem in recent years [1,2]. Developing low-energy techniques that can efficiently generate large-scale fresh water by using the abundance of brackish or sea water on earth [3–5] is believed to be a promising approach to solve this serious problem. Interest in the use of brackish water with salinity between 0.5 and 30 g/L is growing. Conventional desalination technologies such as reverse osmosis, electrodialysis, multi-effect distillation, and multi-stage flash evaporation are just a few of the technologies that have been suggested for this purpose. However, their widespread use has been constrained thus far by their high energy consumption and complex operation [6].

Capacitive deionization (CDI) emerged as the most promising method among a variety of desalination technologies because it is one of the most reliable and affordable methods for desalinating water [7]. The advantages of CDI over other conventional technologies include low operation voltage, high salt removal capacity, minimal chemical demand, and the absence of secondary wastes. The foundation of CDI is the application of an external electrostatic field between electrodes to drive charged species toward electrodes with opposing charges. When the voltage is short-circuited or reversed, charged ions are released from the electrodes, and the electrode is regenerated for cycle use. The electrical double layer (EDL) that forms between the solution and electrode contact can attract and hold the charged species. The EDL capacity as a result of the electrostatic attraction force between the ions and the electrode is a crucial factor contributing to the adsorption capacity of capacitive deionization (CDI) [8–10]. Therefore, the salt adsorption capacity (SAC) of the carbon

electrodes is often limited by both the available surface area and pore structure [11]. Therefore, the theoretical maximum desalination capacities of conventional CDI cells were only ~10–15 $mg \cdot g^{-1}$. Many researchers have concentrated on intercalation-type pseudocapacitive materials or Faradaic materials that react with the ions in a solution to continue Faradic reactions in order to get around the SAC limitation of carbon electrodes [12,13]. Pseudocapacitance, or the features of metal oxide capacitance, results from the lattice spacing that allows for ion storage during faradaic electron transit in various metal states. Currently, two-dimensional (2D) transition metal nitrides/carbides (MXene) are one of the materials with the most potential for electrode use in CDI due to its high electrical conductivity and hydrophilic surfaces, and good ion intercalation–deintercalation reversibility in aqueous media [14]. The layered MAX phases ($M_{n+1}AX_n$) (where M is an early transition metal, A is a group A element (usually Al or Si), X is carbon and/or nitrogen, and n = 1, 2, or 3) are used to create MXenes by etching out the A layer. MXenes are represented as $M_{n+1}X_nT_x$, where x is the number of terminating groups and T refers to the surface termination groups (−O, −OH, and −F) left behind after the etching process. Furthermore, T acts as active sites for crystallization and is beneficial for conductivity, ion insertion, and the extraction process, leading to the improved electrochemical performance. Due to their qualities, they can be employed as great pseudocapacitors to significantly enhance the electrochemical performance and desalination performance of electrode materials [15,16] as well as perfect conducting strips to couple discrete Faradaic or pseudocapacitive materials. For the first time, Srimuk et al. suggested using Ti_3C_2-MXene as the CDI electrode material, with a desalination capacity of 13 $mg \cdot g^{-1}$ [17]. Even though the capacity is somewhat low due to the multilayer structure caused by the lack of a delamination process, it demonstrates that MXene can be employed for CDI as a novel intercalation-type pseudocapacitive electrode. Instead of Ti_3C_2-MXene, Srimuk et al. tested $Mo_{1.33}C$-MXene electrodes, which have a 15 $mg \cdot g^{-1}$ capacity [18]. Although the above MXene electrode performs desalination more effectively than a carbon electrode, the adsorption capacity of MXene is still not very great.

To enhance the electrochemical energy storage performance, intercalation-type pseudocapacitive electrode materials are incorporated to increase the surface area and provide additional pseudocapacitance, such as manganese dioxide (MnO_2) [19–21], Prussian blue and its analogs [22–24], $Na_3V_2(PO_4)_3$ [25], Co_3O_4 [26], Fe_3O_4 [27], and $NaTi_2(PO_4)_3$ (NTP) [28]. One of these materials, MnO_2, is particularly interesting for research because it is widely available, inexpensive, and has good cycle stability [29]. Theoretically, MnO_2 has a substantially larger capacitance (1370 $F \cdot g^{-1}$) than materials based on carbon. Manganese dioxides can be categorized into various crystalline phases depending on the orientation of the MnO_6 octahedra and lattice defects, such as α-MnO_2 (hollandite), β-MnO_2 (pyrolusite), R-MnO_2 (ramsdellite), γ-MnO_2 (intergrowth of and R), and δ-MnO_2 (birnessite). Electrodes containing MnO_2 intercalation typically have a higher ion adsorption capacity than porous carbon materials alone. However, with the exception of a few unique situations with incredibly low loading of the active material, the specific capacitance of MnO_2 measured experimentally is significantly lower than the theoretical value. The discrepancy has been attributed to the poor electrical conductivity and limited surface area of MnO_2, which places a restriction on the pseudocapacitive capability of material. To enhance the performance, forming MnO_2-based hybrid structures with conductive materials is a promising implementation approach. Therefore, combining the positive characteristics of MnO_2 and MXene is an effective strategy for improving the specific capacitance, rate performance, and cycle life of electrode materials. MnO_2/Mxene composites have recently been created by numerous researchers and effectively employed in supercapacitors [30–32], batteries [33], catalysis [34], the removal of heavy metal ions [35,36], and other fields. However, no previous study has used MXene/MnO_2 composite materials as electrodes for achieving desalination through electrosorption.

Herein, we demonstrate a novel strategy for loading MnO_2 on MXene to obtain a MnO_2/MXene composite that exhibits the advantageous characteristics of both MnO_2 and MXene. These qualities include the high electrical conductivity of MXene, which

helps MnO_2 transfer charges more effectively, and the large theoretical capacitance of MnO_2, which supports reversible ion intercalation and deintercalation for high desalination rates and capacities. Simultaneously, the structure and morphology of the MnO_2/MXene composite was characterized by X-ray diffraction (XRD), field-emission scanning electron microscopy (FESEM), and X-ray photoelectron spectra (XPS). Furthermore, the desalination and electrochemical performance of the MnO_2/MXene electrode was carefully studied.

2. Experimental Section

2.1. Materials

All chemicals were purchased from Sinopharm Chemical Reagent Co., Ltd. (Shanghai, China) in analytical purity and used in the experiments directly without any further purification. Ti_3AlC_2 MAX was purchased from Jilin 11 Technology Co., Ltd. (Changchun, China). All the solutions were prepared in high-purity de-ionized water (DIW).

2.2. Synthesis

2.2.1. Synthesis of the Ti_3C_2 MXene

Delaminated $Ti_3C_2T_x$ was prepared by etching Ti_3AlC_2. A total of 2 g of LiF (98.5%) was added to 30 mL of HCl solution (9 M), and 2 g of Ti_3AlC_2 was added to the above solution under stirring for 48 h at 40 °C. Then, the mixture was washed with water using centrifugation until the pH of the supernatant was above 6. The dark green supernatant was collected to obtain the delaminated MXene suspension. This MXene suspension was filtered to measure the concentration of the delaminated MXene. Delaminated $Ti_3C_2T_x$ was then obtained by freeze-drying.

2.2.2. Synthesis of MnO_2/MXene

A total of 2 mL 0.02 mol/L $MnSO_4 \cdot H_2O$ aqueous solution was slowly dropped into 25 mL 0.04 mol/L $KMnO_4$ aqueous solution and stirred for 10 min. The 80 mL (2 mg/mL) MXene colloidal solution was added into the above mixed solution, ultrasonicated for 10 min. The dispersion was transferred to a Teflon-lined stainless-steel autoclave for hydrothermal reaction at 140 °C for 2 h. The MnO_2/MXene product was washed by vacuum filtration with DIW. The washed materials were collected after vacuum drying at 40 °C for 24 h.

2.2.3. Characterization

The samples microstructure analysis was conducted with scanning electron microscopy (SEM, MIRA4 LMH, TESCAN, Brno, Czech Republic). Further, relative contents of elements were figured out using energy dispersive spectrometer (EDS, Ultim Max 40, TESCAN) and mapping. An X-ray diffractometer (XRD, D8 Advance, Bruker, Billerica, MA, USA) was utilized to characterize the composition and crystallographic structure. The surface areas and pore diameters were calculated by the Brunauer–Emmett–Teller (BET, ASAP 2460, Micromeritics) method. Elements were studied by an X-ray photoelectron spectroscopy (XPS, Escalab 250Xi, Thermo Scientific, Bend, OR, USA) using an A1 Kα X-ray source at a pass energy of 160 eV for survey scans and 40 eV for higher solution scans.

2.2.4. Electrochemical Measurement

The cyclic voltammetry (CV), galvanostatic charge–discharge (GCD), and electrochemical impedance spectroscopy (EIS) were measured in 1 M NaCl solution by Metrohm Ltd. (Multi Autolab M204, Herisau, Switzerland) electrochemical workstation. The three-electrode system consists of a MnO_2/MXene electrode (working electrode), an activated carbon electrode (counter electrode), and a Ag/AgCl (3 M KCl) electrode (reference electrode). The working electrodes were fabricated starting with mixing the MnO_2/MXene materials, polyvinylidene difluoride (PVDF), and carbon black with a mass ratio of 80:15:5, all dispersed in N-methyl-2-pyrrolidone (NMP). Then, the obtained slurry was coated on

a carbon paper with a size of 2 cm × 1 cm and then dried at 60 °C for 6 h. The specific capacitance of the electrodes was determined by Equation (1),

$$C_s = \frac{1}{2\mathrm{v} \times \mathrm{m} \times \Delta V} \int IdV \quad (1)$$

where C_s is specific capacitance ($F \cdot g^{-1}$), $\int IdV$ is the integrated area of the CV curve (AV), and ΔV is potential difference window (V), ν is potential scan rate ($V \cdot s^{-1}$), and m is the mass of electrode material (g).

2.2.5. Desalination Performance Experiments

The electrode materials of the cathode and anode were MnO_2/MXene and activated carbon, respectively. A total volume of 40 mL of NaCl solution was continuously circulated within a homemade CDI cell through a peristaltic pump at a flow rate of 10 mL min^{-1}. The CDI cell was composed of a pair of electrodes separated by a silica gel gasket and acrylic plate. The cathode and anode used were, respectively, composed of MnO_2/MXene and AC (activated carbon) with the distance of 1.0 mm. The desalination experiments were conducted at a constant cell voltage of 1.2 V with a starting NaCl concentration ranging from 50 to 5000 mg L^{-1} (0.85–85.5 mM). The salt concentration change was measured by monitoring the effluent conductivity with a DDSJ-308A conductivity meter (INESA Scientific Instrument Co., Shanghai, China). After the effluent conductivity decreased to a constant, the electrodes were then regenerated by applying an inversed voltage until the effluent conductivity was constant. The desalination capacity (Γ) is calculated as follows.

The salt adsorption capacity (SAC $mg \cdot g^{-1}$) was calculated according to the following formulas:

$$SAC = \frac{(C_0 - C_e) \times \mathrm{V}}{\mathrm{m}} \quad (2)$$

where V is the volume of circulated solution (L), C_0 ($mg \cdot L^{-1}$) and C_e ($mg \cdot L^{-1}$) are the initial and equilibrium concentrations of ions, respectively, and m is the mass of a pair of electrodes (g).

3. Results and Discussion

3.1. Materials Characterization

Figure 1 schematically depicts the MnO_2/MXene composite preparation process. To begin with, stacked-layer structured Ti_3C_2 MXene (m-$Ti_3C_2T_x$) was produced by etching layered Ti_3AlC_2 MAX with LiF/HCl while stirring to remove the Al layers and widen the interlayer space of the MAX phase [37]. Then, the m-$Ti_3C_2T_x$ was delaminated by centrifuging to obtain the delaminated MXene. Moreover, MnO_2 was grown on MXene using the hydrothermal method, and the MnO_2/MXene composite was then successfully synthesized. The morphologies of the prepared MXene and MnO_2/MXene composite were investigated via field-emission scanning electron microscopy (FESEM). Figure 1 shows that multilayer $Ti_3C_2T_x$ becomes few-layered or even single-layered after the ultrasonic delamination process. The irregular particle MnO_2 was grown over the MXene 2D layers (Figure 2b), which act as a conducting layer coupling each individual MnO_2 particle, thus forming a plane-to-line ($Ti_3C_2T_x$-to-MnO_2) conducting network. The elemental analysis was performed on the MnO2/MXene composite using energy-dispersive X-ray spectroscopy (EDS). The Mn:O ratio is 1:2.2, confirming the formation of MnO_2. A slightly higher O content than 1:2 is due to the presence of TiO_2 which agreed well with the XRD result. However, the Ti:O ratio is 2.27:1, which indicates that the content of Ti is much higher than O, and the TiO_2 is only very little. The formation of the MnO_2/MXene composites was also verified via an elemental mapping analysis (Figure 2). The Mn, Ti, and O signals were found to be uniformly distributed based on the MnO_2 and MXene on the surface of the MnO_2/MXene composite. The successful and tight adhesion of MnO_2 to the $Ti_3C_2T_x$ surface is thus demonstrated.

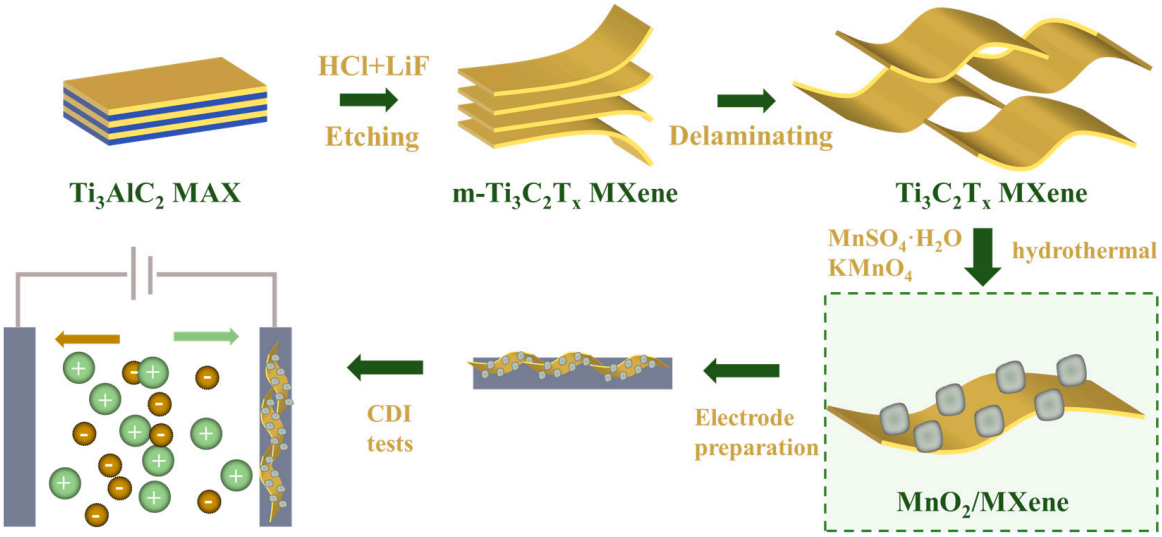


Figure 1. Schematic of the synthesis of the composites and their application in CDI.

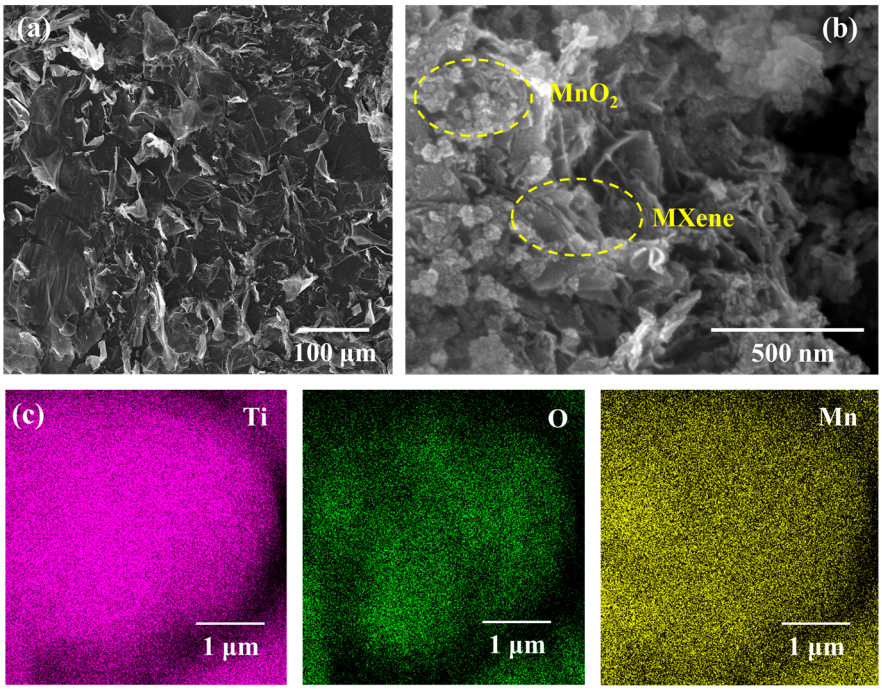


Figure 2. (**a**,**b**) FESEM images of MXene and MnO_2/MXene and (**c**) with the corresponding EDS elemental mappings of Mn, O, and Ti.

A more detailed phase structure of the MnO_2/MXene composite was studied via XRD analysis (Figure 3a); the diffraction peaks of MnO_2/MXene are too broad to be detected with low intensity, which is probably ascribed to its lower crystallinity. Moreover, the weak characteristic peak corresponding to TiO_2 was observed in the XRD pattern of the MnO_2/MXene composite, suggesting that the MXene was oxidated during fabricating the composite. The surface chemical composition and chemical valence states of the MnO_2/MXene composite were analyzed via XPS. The survey spectra of the MnO_2/MXene composite shows the characteristic peaks of C 1s (285 eV), O 1s (530 eV), Ti 2p (458 eV), and Mn 2p (643 eV) (Figure 3b). The MnO_2 phase is present in the composite and is consistent with the XRD data because the value of the Mn 2p peaks with a spin-energy separation of 11.8 eV indicates that the main oxidation state of Mn is +4 (Figure 3c). [30]. Figure 3d shows the high-resolution Ti 2p XPS spectra of the MnO_2/MXene composite. The $2p_{3/2}$ and $2p_{1/2}$

orbits of Ti^{3+} in the MXene are located at 457.8 and 463.2 eV, respectively. Additionally, the peaks at 455.9 and 462.2 eV can be attributed to the Ti–O ($2p_{3/2}$) and Ti–O ($2p_{1/2}$) bonds, respectively, which originate from the oxygen-containing groups attached to the surface of the MXene. These XPS results indicate that MXene is present in the MnO_2/MXene composite. Moreover, as observed from the high-resolution Ti 2p XPS spectra of the MnO_2/MXene composite, the contents of Ti^{2+} and Ti^{3+} are larger than Ti–O, indicating that Ti_3C_2 MXene partially oxidized to TiO_2. The reason the Ti_3C_2 MXene peaks were not detected by the XRD is maybe the low content. To investigate the pore structure of the MnO_2/MXene composite, their nitrogen adsorption–desorption was measured, and the corresponding isotherm is shown in Figure 3e. The sample displays significant hysteresis loops between 0.45 and 1.0 P/P_0, demonstrating the existence of a mesoporous structure. The pore-size distributions of the samples calculated from the desorption isotherms using the Barret–Joyner–Halenda (BJH) method are shown in the inset of Figure 3e. The majority of the pores of MnO_2/MXene lie in the range of 8–12 nm. As a result, the mesoporous MnO_2/MXene composite is predicted to have good electrochemical characteristics [38]. The BET surface area calculated for MnO_2/MXene is 184.59 m^2/g.

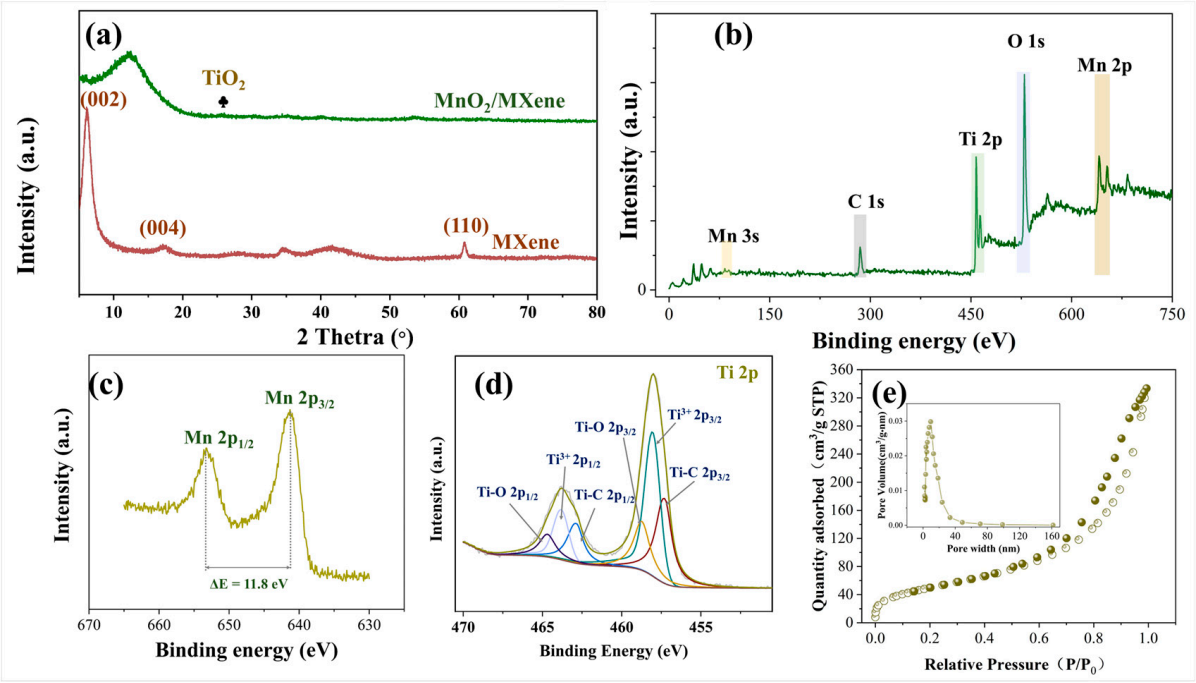


Figure 3. (**a**,**b**) XRD patterns and XPS survey spectra of MnO_2/MXene composites, (**c**,**d**) high-resolution Mn 2p and Ti 2p XPS spectra, (**e**) nitrogen adsorption–desorption isotherms and pore diameter distribution of MnO_2/MXene.

3.2. Desalination Performance

Figure 4a shows the desalination capacity of MnO_2/MXene in a solution with an initial charge concentration of 1000 $mg \cdot L^{-1}$ at 1.2 V. The rapid desalting phase is 5 min, and the desalination capacity is over 50% of the maximum desalination capacity, and then the desalination capacity continues to increase with a slow absorption rate of 5–60 min. The maximum desalination capacity is 30.25 mg g^{-1} for the total mass of active materials, which is higher than those of the reported pure $Ti_3C_2T_x$ (13.58 mg g^{-1}) [17] and MnO_2 electrode (9.93 mg g^{-1}) [39]. Further experiments were conducted in solutions with various concentrations (Figure 4b). Langmuir and Freundlich isotherms were used to validate the experimental data. The Freundlich model ($R^2 > 0.9829$) fits better than the Langmuir model ($R^2 > 0.8866$), which indicates a multilayer adsorption mechanism on the MnO_2/MXene.

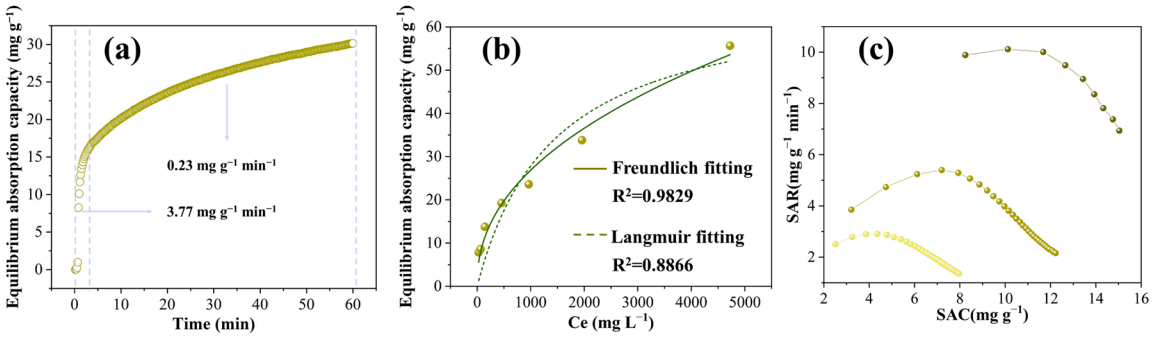


Figure 4. Desalination performance. (**a**) Electrosorption curves obtained using a NaCl solution (concentration: 1000 mg L^{-1}), (**b**) fitting curves obtained using the Langmuir model, (**c**) Ragone plots at various operating concentrations.

Ragone plots, which carefully balance the SAC and ion adsorption rate, were used to further demonstrate the desalination performance of the MnO_2/MXene electrodes (SAR). Figure 4c shows that the MnO_2/MXene curves shift in the upper right direction with increasing initial concentration. This shows that when the concentration rose, the ionic conductivity increased, creating circumstances that made the rapid passage of ions to the electrode more likely; therefore, the MnO_2/MXene electrodes show excellent desalination and rate performance. Additionally, MnO_2/MXene (3.77 mg g^{-1} min^{-1}) exhibits a higher desalination rate than $Ti_3C_2T_x$ (0.91 mg g^{-1} min^{-1}). This is due to the composite structure of the MnO_2 and $Ti_3C_2T_x$ in which MXene can provide a conductive channel for ultrafast electron transport [40]. The high desalination rate of the MnO_2/MXene electrode in this work strongly suggests that it has a good kinetic performance, which is crucial in the actual desalination process [41]. Based on the above analysis, the excellent desalination performance and electrochemical performance of the MnO_2/MXene electrode can be attributed to the following reasons.

(1) Owing to its excellent conductivity, MXene provides an electron conduction highway network for MnO_2, forming a plane-to-point conduction network, which not only considerably improves the ability of MnO_2 to participate in desalination but also effectively reduces the ion diffusion path, affording a high desalination capacity, a rapid desalination rate, and improved electrochemical desalination reaction kinetics.

(2) The low-crystallinity ε-MnO_2 and δ-MnO_2, as confirmed via XRD, have abundant grain boundaries and ion diffusion channels owing to their disordered structure, which considerably improves the electrochemical performance.

(3) MXene can store charge through the double-layer principle by relying on surface ion adsorption, thereby providing an effective capacitance contribution, which is conducive to improving the desalination performance.

3.3. Electrochemical Properties

The electrochemical properties of the as-prepared MnO_2/MXene electrode were evaluated via CV and GCD tests using a three-electrode system in a 1 M NaCl solution. Figure 5a shows the CV curves of the MnO_2/MXene electrode at different scan rates in a fixed potential range from −0.1 to 0.3 V. Clearly, the MnO_2/MXene electrode exhibits pseudo-rectangular-shaped CV curves without obvious redox peaks, strongly suggesting the simultaneous contribution of the electrical double-layer formation and Faradaic redox process to the specific capacitance of the present materials. Moreover, the shape of the CV curves tends to change from quasi-rectangular to spindle, indicating the occurrence of a rapidly reversible Faradaic reaction for pseudocapacitive materials [42,43], which is favorable for enhancing the desalination capacity. With the increase in the scan rate, symmetric oxidation and reduction peaks can be observed at a scan rate as high as 100 mV s^{-1} for the MnO_2/MXene, indicating the excellent reversibility of this electrode.

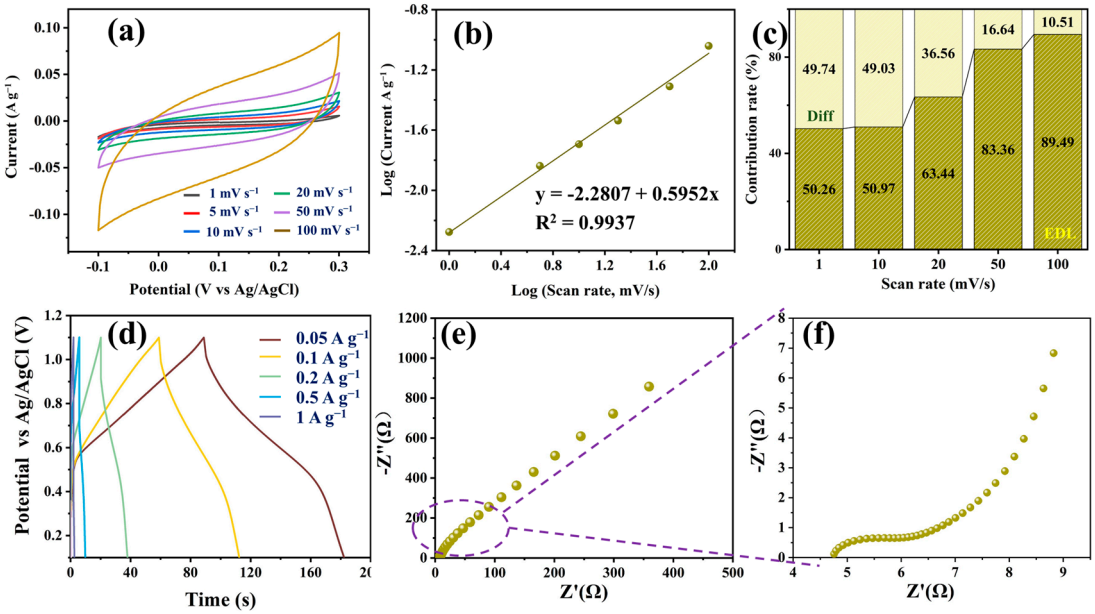


Figure 5. Electrochemical properties. (**a**) CV curves; (**b**) log-log plots; (**c**) capacitive and diffusion-controlled contributions at different scan rates; (**d**) GCD curves; (**e**,**f**) EIS spectra.

To further investigate the electrochemical kinetics and charge storage mechanisms of the two electrodes, the capacitive and diffusion contributions to the current response are quantitatively evaluated. The two-phase charge control can be determined based on the relationship between the measured current (i) and the scan rate (v) from the CV curves [44]:

$$i = av^b, \tag{3}$$

$$\log(i) = b\log(v) + \log(a), \tag{4}$$

where a and b are constants. On composite charge storage devices, b values are typically employed to evaluate the partial impact of electrochemical double-layer capacitors or pseudocapacitors. This behavior resembles that of a battery because when the proton bulk transport mechanism occurs and the b value just misses 0.5 at a lower voltage, a diffusion-controlled redox reaction occurs. Because the responsive current is dominated by the surface capacitive contribution when the b value approaches 1 with a further increase in potential, the behavior is similar to that of a supercapacitor and includes both double-layer capacitive and surface redox reactions. At b = 1, fast capacitive charge storage is expected, whereas b = 0.5 implies that the current flow is governed by a diffusion-limited process [45]. The b value for MnO_2/MXene is 0.5952 (Figure 5e), indicating both the capacitive contribution and diffusion-controlled contribution for the MnO_2/MXene electrode. The contributions of the two processes to the total capacitance are further calculated (Figure 5f) by analyzing the current response at a particular potential based on Dunn's method [46,47]:

$$i(V) = k_1 v + k_2 v^{0.5} \tag{5}$$

where $k_1 v$ and $k_2 v^{0.5}$ account for the capacitive and the diffusion-controlled processes (charge transfer), respectively. The slope and interception represent the k_1 and k_2 values, respectively. The plots in Figure 5c clearly show that the percentage of the capacitive contribution increases from 50.26% to 89.49% for the MnO_2/MXene electrode with an increasing scan rate. This is because redox reactions are limited at high scan rates; thus, the diffusion-controlled process becomes negligible, whereas the capacitive process contributes more to the capacitance as the scan rate increases. Further, of the MnO_2/MXene electrode, the capacitive process contributes approximately 50.3% of the total capacitance according

to Trasatti's method [48]. This indicates the occurrence of possible violent redox reactions in the MnO_2/MXene electrode. This result further proves that the electrochemical activity of the MnO_2/MXene electrode is due to the EDLC and the ion intercalation reactions. Interestingly, the surface area of MnO_2/MXene is larger than other reported samples, while the capacitive process contribution and diffusion control contribution are basically the same, which further indicates the occurrence of violent redox reactions in the MnO_2/MXene electrode. Thus, MnO_2/MXene is a pseudocapacitive electrode that may remove Na^+ ions through intercalation/deintercalation along with the Faradaic redox reaction in the transformation of the +4 and +3 oxidation states of Mn (Equation (6)) [49].

$$(MnO_2) + Na^+ + e^- \leftrightarrow MnOONa \quad (6)$$

The GCD curves of the two MnO_2/MXene electrodes at current densities from 0.05 to 1 A g^{-1} are shown in Figure 5d. All the GCD curves are the nearly symmetric shape of the charge–discharge curves recorded at different current densities, indicating the fast ion transport within the electrodes, superior reversible redox reaction, and good electrochemical capacitive characteristic. Additionally, at the start of the discharge curve, these charge–discharge curves show a very small voltage, indicating the very low inner resistance and ion diffusion resistance between the electrode material and salt electrolyte [50]. Therefore, in this composite, the enhancement of the charge storage capacity is significantly dependent on the effective charge transfer at the interface between the MXene and MnO_2.

EIS measurements were performed to investigate the electrochemical properties of the electrode in detail. The EIS results of the MnO_2/MXene electrode are shown in Figure 5e. A curve shows an Ohmic capacitance resistance in the high-frequency region and a diffusion tail in the low-frequency region, which correspond to the charge transfer (R_{ct}) and ion diffusion processes, respectively. Small semicircles are related to low R_{ct}. The R_{ct} value of the MnO_2/MXene electrode is 0.804 Ω, suggesting fast charge transport for both electrodes. The low-frequency line of the MnO_2/MXene electrode is subvertical, implying a small Warburg impedance and good capacitance characteristics. Such an excellent electrochemical performance makes us more interested in exploring their application in CDI and then laying the foundation for practicality.

4. Conclusions

In the current study, MnO_2 was successfully loaded on MXene to obtain a MnO_2/MXene composite. The obtained MnO_2/MXene composite exhibited low crystallinity and good electrochemical performance. As demonstrated, MnO_2/MXene exhibits a better desalination performance than the reported pure MnO_2 and MXene electrode materials, including a maximum deionization rate of 3.77 mg g^{-1} min^{-1} and a desalination capacity of 30.25 mg·g^{-1}. The EDL capacitive and the diffusion-controlled processes are the main charge/ion storage mechanisms, and the capacitive contribution provides 50.3% to the total capacitance. These results provide insight into the electrochemical adsorption mechanism of the MnO_2/MXene electrode and offer guidance to further improve their desalination capacity.

Author Contributions: Z.S.: Data curation, Formal Analysis, Writing—original draft; J.P.: Software, Visualization; S.Y.: Investigation, Methodology; R.J.: Conceptualization, Resources.; C.L.: Funding Acquisition, Project Administration; Q.H.: Supervision, Validation, Writing—Review and Editing. All authors have read and agreed to the published version of the manuscript.

Funding: This work was supported by the National Natural Science Foundation of China [52004035] and the China Postdoctoral Science Foundation [2021M703651].

Data Availability Statement: Not applicable.

Conflicts of Interest: The authors declare no conflict of interest.

References

1. Shannon, M.; Bohn, P.; Elimelech, M.; Georgiadis, J.; Marinas, B.; Mayes, A. Science and technology for water purification in the coming decades. *Nature* **2008**, *452*, 301–310. [CrossRef] [PubMed]
2. Elimelech, M.; Phillip, W. The future of seawater desalination: Energy, technology, and the environment. *Science* **2011**, *333*, 712–717. [CrossRef] [PubMed]
3. Gleick, P. *Water in Crisis: A Guide to the World's Fresh Water Resources*; Oxford University Press: New York, NY, USA, 1993.
4. Tang, K.; Hong, T.; You, L.; Zhou, K. Carbon-metal compound composite electrodes for capacitive deionization: Synthesis, development and applications. *J. Mater. Chem. A* **2019**, *7*, 26693–26743. [CrossRef]
5. McGovern, R.; Weiner, A.; Sun, L.; Chambers, C.; Zubair, S.; Lienhard, V.J. On the cost of electrodialysis for the desalination of high salinity feeds. *Appl. Energy* **2014**, *136*, 649–661. [CrossRef]
6. Porada, S.; Zhao, R.; van der Wal, A.; Presser, V.; Biesheuvel, P. Review on the science and technology of water desalination by capacitive deionization. *Prog. Mater. Sci.* **2013**, *58*, 1388–1442. [CrossRef]
7. Wang, R.; Sun, K.; Zhang, Y.; Qian, C.; Bao, W. Dimensional optimization enables high-performance capacitive deionization. *J. Mater. Chem. A* **2022**, *1*, 6414–6441. [CrossRef]
8. Xu, X.; Yang, T.; Zhang, Q.; Xia, W.; Ding, Z.; Eid, K.; Abdullah, A.; Hossain, M.; Zhang, S.; Tang, J.; et al. Ultrahigh capacitive deionization performance by 3D interconnected MOF-derived nitrogen-doped carbon tubes. *Chem. Eng. J.* **2020**, *390*, 124493. [CrossRef]
9. Li, Y.; Ding, Z.; Zhang, X.; Li, J.; Liu, X.; Lu, T.; Yao, Y.; Pan, L. Novel hybrid capacitive deionization constructed by a redox-active covalent organic framework and its derived porous carbon for highly efficient desalination. *J. Mater. Chem.* **2019**, *7*, 2535–25313. [CrossRef]
10. Feng, C.; Tsai, C.; Ma, C.; Yu, C.; Hou, C. Integrating cost-effective microbial fuel cells and energy-efficient capacitive deionization for advanced domestic wastewater treatment. *Chem. Eng. J.* **2017**, *330*, 1–10. [CrossRef]
11. Wu, T.; Wang, G.; Wang, S.; Zhan, F.; Fu, Y.; Qiao, H.; Qiu, J. Highly Stable Hybrid Capacitive Deionization with a MnO_2 Anode and a Positively Charged Cathode. *Environ. Sci. Tech. Let.* **2018**, *5*, 98–102. [CrossRef]
12. Pasta, M.; Wessells, C.; Cui, Y.; La Mantia, F. A desalination battery. *Nano Lett.* **2012**, *12*, 839–843. [CrossRef] [PubMed]
13. Jin, J.; Li, M.; Tang, M.; Li, Y.; Liu, Y.; Cao, H.; Li, F. Phase- and Crystallinity-Tailorable MnO_2 as an Electrode for Highly Efficient Hybrid Capacitive Deionization (HCDI). *ACS Sustain. Chem. Eng.* **2020**, *8*, 11424–11434. [CrossRef]
14. Bo, Z.; Yi, K.; Yang, H.; Guo, X.; Huang, Z.; Zheng, Z.; Yan, J.; Cen, K.; Ostrikov, K. More from Less but Precise: Industry-relevant Pseudocapacitance by Atomically-precise Mass-loading MnO_2 within Multifunctional MXene Aerogel. *J. Power Sources* **2021**, *492*, 229639. [CrossRef]
15. Zhang, B.; Boretti, A.; Castelletto, S. Mxene pseudocapacitive electrode material for capacitive deionization. *Chem. Eng. J.* **2022**, *435*, 134959. [CrossRef]
16. Dixit, F.; Zimmermann, K.; Dutta, R.; Prakash, N.; Barbeau, B.; Mohseni, M. Kandasubramanian, Application of MXenes for Water Treatment and Energy-Efficient Desalination: A Review. *J. Hazard. Mater.* **2022**, *423*, 127050. [CrossRef] [PubMed]
17. Srimuk, P.; Kaasik, F.; Krüner, B.; Tolosa, A.; Fleischmann, S.; Jäckel, N.; Tekeli, M.; Aslan, M.; Suss, M.; Presser, V. MXene as a novel intercalation-type pseudocapacitive cathode and anode for capacitive deionization. *J. Mater. Chem. A* **2016**, *4*, 18265–18271. [CrossRef]
18. Srimuk, P.; Halim, J.; Lee, J.; Tao, Q.; Rosen, J.; Presser, V. Two-Dimensional Molybdenum Carbide (MXene) with Divacancy Ordering for Brackish and Seawater Desalination via Cation and Anion Intercalation. *ACS Sustain. Chem. Eng.* **2018**, *6*, 3739–3747. [CrossRef]
19. Kim, S.; Lee, J.; Kang, J.; Jo, K.; Kim, S.; Sung, Y.; Yoon, J. Lithium recovery from brine using a lambda-MnO_2/activated carbon hybrid supercapacitor system. *Chemosphere* **2015**, *125*, 50–56. [CrossRef]
20. Byles, B.; Hayes-Oberst, B.; Pomerantseva, E. Ion Removal Performance, Structural/Compositional Dynamics, and Electrochemical Stability of Layered Manganese Oxide Electrodes in Hybrid Capacitive Deionization. *ACS Appl. Mater. Inter.* **2018**, *10*, 32313–32322. [CrossRef]
21. Hand, S.; Cusick, R. Characterizing the Impacts of Deposition Techniques on the Performance of MnO_2 Cathodes for Sodium Electrosorption in Hybrid Capacitive Deionization. *Environ. Sci. Technol.* **2017**, *51*, 12027–12034. [CrossRef]
22. Guo, L.; Mo, R.; Shi, W.; Huang, Y.; Leong, Z.; Ding, M.; Chen, F.; Yang, H. A Prussian blue anode for high performance electrochemical deionization promoted by the faradaic mechanism. *Nanoscale* **2017**, *9*, 13305–13312. [CrossRef] [PubMed]
23. Ding, Z.; Xu, X.; Li, Y.; Wang, K.; Lu, T.; Pan, L. Significantly improved stability of hybrid capacitive deionization using nickel hexacyanoferrate/reduced graphene oxide cathode at low voltage operation. *Desalination* **2019**, *468*, 114078. [CrossRef]
24. Lee, J.; Kim, S.; Yoon, J. Rocking Chair Desalination Battery Based on Prussian Blue Electrodes. *ACS Omega* **2017**, *2*, 1653–1659. [CrossRef]
25. Cao, J.; Wang, Y.; Wang, L.; Yu, F.; Ma, J. $Na_3V_2(PO_4)_3$@C as Faradaic Electrodes in Capacitive Deionization for High-Performance Desalination. *Nano Lett.* **2019**, *19*, 823–828. [CrossRef] [PubMed]
26. Zhang, Y.; Hu, Y.; Wang, Z.; Lin, T.; Zhu, X.; Luo, B.; Hu, H.; Xing, W.; Yan, Z.; Wang, L. Lithiation-Induced Vacancy Engineering of Co_3O_4 with Improved Faradic Reactivity for High-Performance Supercapacitor. *Adv. Funct. Mater.* **2020**, *30*, 2004172. [CrossRef]
27. Trinh, N.; Chung, S.; Lee, J.; Lee, J. Development of high quality Fe_3O_4/rGO composited electrode for low energy water treatment. *J. Energy Chem.* **2016**, *25*, 354–360. [CrossRef]

28. Liang, S.; Han, C.; Meng, Q.; Tian, G. Nitrogen and sulfur co-doped $NaTi_2(PO_4)_3$/hole graphene composite as high-performance electrosorption electrodes for hybrid capacitive deionization. *J. Mater. Sci.* **2020**, *55*, 6017–6029. [CrossRef]
29. Yuan, Y.; Yao, W.; Byles, B.; Pomerantseva, E.; Amine, K.; Shahbazian-Yassar, R.; Lu, J. Revealing the Atomic Structures of Exposed Lateral Surfaces for Polymorphic Manganese Dioxide Nanowire. *Small Struct.* **2021**, *2*, 91. [CrossRef]
30. Li, X.; Zhu, J.; Zhang, B.; Jiao, Y.; Huang, J.; Wang, F. Manganese dioxide nanosheets decorated on MXene (Ti_3C_2Tx) with enhanced performance for asymmetric supercapacitors. *Ceram. Int.* **2021**, *47*, 12211–12220. [CrossRef]
31. Chen, S.; Xiang, Y.; Xu, W.; Peng, C. A novel MnO_2/MXene composite prepared by electrostatic self-assembly and its use as an electrode for enhanced supercapacitive performance. *Inorg. Chem. Front.* **2019**, *6*, 199–208. [CrossRef]
32. Rakhi, R.; Ahmed, B.; Anjum, D.; Alshareef, H. Direct Chemical Synthesis of MnO_2 Nanowhiskers on Transition-Metal Carbide Surfaces for Supercapacitor Applications. *ACS Appl. Mater. Interfaces* **2016**, *8*, 18806–18814. [CrossRef] [PubMed]
33. Qi, M.; Li, F.; Zhang, Z.; Lai, Q.; Liu, Y.; Gu, J.; Wang, L. Three-dimensional interconnected ultrathin manganese dioxide nanosheets grown on carbon cloth combined with $Ti_3C_2T_x$ MXene for high-capacity zinc-ion batteries. *J. Colloid Interf. Sci.* **2022**, *615*, 151–162. [CrossRef] [PubMed]
34. Zhu, L.; Lv, J.; Yu, X.; Zhao, H.; Sun, C.; Zhou, Z.; Ying, Y.; Tan, L. Further construction of MnO_2 composite through in-situ growth on MXene surface modified by carbon coating with outstanding catalytic properties on thermal decomposition of ammonium perchlorate. *Appl. Surf. Sci.* **2020**, *502*, 144171. [CrossRef]
35. Khan, A.; Awan, S.; Husnain, S.; Abbas, N.; Anjum, D.; Abbas, N.; Benaissa, M.; Mirza, C.; Mujtaba-ul-Hassan, S. Shahzad, 3D flower like 8-MnO_2/MXene Nano-hybrids for the removal of hexavalent Cr from wastewater. *Ceram. Int.* **2021**, *47*, 25951–25958. [CrossRef]
36. Qu, H.; Deng, J.; Peng, D.; Wei, T.; Zhang, H.; Peng, R. Selective Adsorption of Pb^{2+} in the Presence of Mg^{2+} by Layer-by-Layer Self-Assembled MnO_2/Mxene Composite Films. *Processes* **2022**, *10*, 641. [CrossRef]
37. Liu, Q.; Yang, J.; Luo, X.; Miao, Y.; Zhang, Y.; Xu, W.; Yang, L.; Liang, Y.; Weng, W.; Zhu, M. Fabrication of a fibrous MnO_2@MXene/CNT electrode for high-performance flexible supercapacitor. *Ceram. Int.* **2020**, *46*, 11874–11881. [CrossRef]
38. Wang, G.; Xu, H.; Lu, L.; Zhao, H. One-step synthesis of mesoporous MnO_2/carbon sphere composites for asymmetric electrochemical capacitors. *J. Mater. Chem. A* **2015**, *3*, 1127–1132. [CrossRef]
39. Leong, Z.; Yang, H. A Study of MnO_2 with Different Crystalline Forms for Pseudocapacitive Desalination. *ACS Appl. Mater. Interfaces* **2019**, *11*, 13176–13184. [CrossRef]
40. Wang, K.; Chen, L.; Zhu, G.; Xu, X.; Wan, L.; Lu, T.; Pan, L. Ferroferric oxide@titanium carbide MXene heterostructure with enhanced sodium storage ability for efficient hybrid capacitive deionization. *Desalination* **2022**, *522*, 115420. [CrossRef]
41. Wang, S.; Li, Z.; Wang, G.; Wang, Y.; Ling, Z.; Li, C. Freestanding Ti_3C_2 Tx MXene/Prussian Blue Analogues Films with Superior Ion Uptake for Efficient Capacitive Deionization by a Dual Pseudocapacitance Effect. *ACS Nano* **2022**, *16*, 1239–1249. [CrossRef]
42. Chen, H.; Zhang, B.; Li, F.; Kuang, M.; Huang, M.; Yang, Y.; Zhang, Y. Sculpturing the Core towards Mesoporous Manganese Dioxides Nanosheets-Built Nanotubes for Pseudocapacitance. *Electrochim. Acta* **2016**, *187*, 488–495. [CrossRef]
43. Simon, P.; Gogotsi, Y. Materials for electrochemical capacitors. *Nat. Mater.* **2008**, *7*, 845–854. [CrossRef] [PubMed]
44. Chao, D.; Liang, P.; Chen, Z.; Bai, L.; Shen, H.; Liu, X.; Xia, X.; Zhao, Y.; Savilov, S.; Lin, J.; et al. Pseudocapacitive Na-Ion Storage Boosts High Rate and Areal Capacity of Self-Branched 2D Layered Metal Chalcogenide Nanoarrays. *ACS Nano* **2016**, *10*, 10211–10219. [CrossRef] [PubMed]
45. Wang, R.; Xu, C.; Lee, J. High performance asymmetric supercapacitors: New NiOOH nanosheet/graphene hydrogels and pure graphene hydrogels. *Nano Energy* **2016**, *19*, 210–221. [CrossRef]
46. Wang, J.; Polleux, J.; Lim, J.; Dunn, B. Pseudocapacitive Contributions to Electrochemical Energy Storage in TiO_2 (Anatase) Nanoparticles. *J. Phys. Chem. C* **2007**, *111*, 14925–14931. [CrossRef]
47. Brezesinski, T.; Wang, J.; Polleux, J.; Dunn, B.; Tolbert, S. Templated nanocrystal-based porous TiO_2 films for next-generation electrochemical capacitors. *J. Am. Chem. Soc.* **2009**, *131*, 1802–1809. [CrossRef]
48. Zhou, Z.; Liu, T.; Khan, A.; Liu, G. Block copolymer-based porous carbon fibers. *Sci. Adv.* **2019**, *5*, u6852. [CrossRef]
49. Liu, Y.; Yu, T.; Chen, Y.; Hou, C. Incorporating Manganese Dioxide in Carbon Nanotube–Chitosan as a Pseudocapacitive Composite Electrode for High-Performance Desalination. *ACS Sustain. Chem. Eng.* **2018**, *6*, 3196–3205. [CrossRef]
50. Hou, D.; Zhang, Q.; Xu, X.; Zhang, J.; Li, W.; Wang, P. Insights on ions migration in the nanometer channel of calcium silicate hydrate under external electric field. *Electrochim. Acta* **2019**, *320*, 134637. [CrossRef]

Disclaimer/Publisher's Note: The statements, opinions and data contained in all publications are solely those of the individual author(s) and contributor(s) and not of MDPI and/or the editor(s). MDPI and/or the editor(s) disclaim responsibility for any injury to people or property resulting from any ideas, methods, instructions or products referred to in the content.